The enhancement and decrement of the Sunyaev-Zel'dovich effect towards the ROSAT Cluster RXJ0658-5557The enhancement and decrement of the Sunyaev-Zeldovich effect towards the ROSAT Cluster RXJ0658-5557

Andreani, P.; Böhringer, H.; Dall'Oglio, G.; Martinis, L.; Shaver, P. A.; Lemke, R.; Nyman, L. A. A.; Booth, R.; Pizzo, L.; Whyborn, N.

Published in:
The Astrophysical Journal

DOI:
10.1086/306830

Publication date:
1999

THE ASTROPHYSICAL JOURNAL, 513:23–33, 1999 March 1

THE ENHANCEMENT AND DECREMENT OF THE SUNYAEV-ZELDOVICH EFFECT TOWARD THE *ROSAT* CLUSTER RX J0658−5557[1]

P. ANDREANI
Dipartimento di Astronomia, Università di Padova, Vicolo Osservatorio 5, I-35122, Padova, Italy; andreani@pd.pd.astro.it
H. BÖHRINGER
Max-Planck Institut für extraterrestrische Physik, Postfach 1603, 85740 Garching bei München, Germany
G. DALL'OGLIO
Dipartimento di Fisica, III Università degli Studi di Roma, Italy; dalloglio@amaldi.fis.uniroma3.it
L. MARTINIS
Energia Nucleare e Energie Alternative, TIB, Frascati, Italy
P. SHAVER
European Southern Observatory, Karl Schwarzchild-Strasse 2, 85748 Garching bei München, Germany; pshaver@eso.org
R. LEMKE AND L.-Å. NYMAN
European Southern Observatory, La Silla, Chile; rlemke@eso.org, lnyman@eso.org
R. BOOTH
ONSALA Space Observatory, S-43992 Onsala, Sweden
L. PIZZO
Dipartimento di Fisica, III Università degli Studi di Roma, Italy; pizzo@amaldi.fis.uniroma3.it
N. WHYBORN
Space Research Organization of the Netherlands (SRON), P.O. Box 800, Groningen, The Netherlands; nick@sron.rug.nl
Y. TANAKA
Astronomical Institute, University of Amsterdam, 1098 SJ Amsterdam, The Netherlands
AND
H. LIANG
Physics Laboratory, University of Bristol, Tyndall Avenue, Bristol BS8 1TL, UK; h.liang@bristol.ac.uk
Received 1998 January 5; accepted 1998 October 8

ABSTRACT

We report simultaneous observations of the X-ray cluster RX J0658−5557 at 1.2 and 2 mm made with a double-channel photometer on the Swedish ESO Submillimeter Telescope (SEST) in search of Sunyaev-Zeldovich (SZ) effect. The SZ data were analyzed using the relativistically correct expression for the Comptonization, and we find $(2.60 \pm 0.79) \times 10^{-4}$ from the detected decrement, which is consistent with that computed using the X-ray (*ROSAT* and *ASCA*) observations. The uncertainty includes contributions from statistical uncertainties in the detection, systematics, and calibration. The 1.2 mm channel data alone give rise to a larger Comptonization parameter; this result is discussed in terms of contamination from foreground sources and/or dust in the cluster or from a possible systematic effect. We then make use of a combined analysis of the *ROSAT* and *ASCA* X-ray satellite observations to determine an isothermal model for the SZ surface brightness. Since the cluster is asymmetrical and probably in a merging process, models are only approximate. The associated uncertainty can, however, be estimated by exploring a set of alternative models. We then find a factor of 1.3 for the global uncertainty on the Comptonization parameter. Combining the SZ and the X-ray measurements, we determine a value for the Hubble constant. The 2 mm data are consistent with $H_0(q_0 = \frac{1}{2}) = 53^{+38}_{-28}$ km s^{-1} Mpc^{-1}, where the uncertainty is dominated by the uncertainty in the models of the X-ray plasma halo.

Subject headings: cosmic microwave background — cosmology: observations — distance scale — galaxies: clusters: individual (RX J0658−5557) — X-rays: galaxies

1. INTRODUCTION

The inverse Compton scattering on the photons of the cosmic microwave background (CMB) by the hot e^- gas residing in rich clusters of galaxies causes an effect known as the Sunyaev-Zeldovich effect (Zeldovich & Sunyaev 1969; Sunyaev & Zeldovich 1972, 1981). The interaction gives rise to a net intensity change with respect to the undistorted blackbody spectrum that has a distinctive behavior as a function of wavelength: it is negative for wavelengths larger than $\lambda_0 = 1.4$ mm (decrement) and positive at shorter wavelengths (enhancement).

The original computation by Sunyaev and Zeldovich of the net transfer of energy from the hot e^- to the microwave photons predicts a signal for the relative temperature change:

$$\left(\frac{\Delta T}{T}\right)_{\rm therm} = y\left(x\,\frac{e^x+1}{e^x-1} - 4\right), \qquad (1)$$

where T is the CMB temperature, $x = h\nu/kT$ and $y = \int (kT_e/mc^2) n_e \sigma_T \, d\ell \simeq (kT_e/mc^2)\tau$ are the Comptonization parameters; n_e, T_e, and m_e are the electron density, tem-

[1] Based on observations made with the ESO-Swedish SEST 15 m telescope (La Silla, Chile).

perature, and mass, respectively, and $\sigma_T = 6.65 \times 10^{-25}$ cm^{-2} is the Thomson cross section. Equation (1) is an approximate solution of the full kinetic equation for the change in the photon distribution caused by scattering. A more accurate solution gives rise to corrections, $\Psi(x, T_e)$, which are not negligible at high frequencies (see Wright 1979; Rephaeli 1995a, 1995b; Challinor & Lasenby 1998):

$$\left(\frac{\Delta T}{T}\right)_{\rm therm} = \left(\frac{e^x - 1}{xe^x}\right)\int d\tau \Psi(x, T_e) \, . \quad (2)$$

If the cluster has a peculiar velocity relative to the frame in which the CMB is isotropic, an additional effect should be measured, generally labeled *kinematic*. The motion of the gas cloud will induce a Doppler change whose relative amplitude, $(\Delta T/T)_{\rm kin}$, depends not on the frequency but only on the peculiar velocity and the cloud optical depth for Thomson scattering, τ; $(\Delta T/T)_{\rm kin} = -(v_r/c)\tau$ (where the minus sign refers to a cluster receding from the observer). Since both effects are very small, the net relative temperature change is just the sum of the two.

The combination of X-ray observations of the thermal bremsstrahlung emission by the hot gas and the radio and millimeter data of the clusters is a powerful cosmological tool for investigating physical processes in the earlier universe, determining H_0 and q_0, the peculiar velocities of clusters, and the nature of the intracluster medium (ICM) (see the original papers by Zeldovich & Sunyaev).

Many observational efforts, mostly in the Rayleigh-Jeans (R-J) part of the spectrum, were carried out with the aim of detecting these effects (see, e.g., the recent reviews by Rephaeli 1995a and Birkinshaw 1997). The expected decrement at centimeter wavelengths is found toward A2218, A665, 0016+16, A773, A401, A478, A2142, A2256, and Coma (Birkinshaw & Gull 1984; Birkinshaw 1991; Klein et al. 1991; Jones et al. 1993; Grainge et al. 1993; Herbig et al. 1995; Carlstrom, Joy, & Grego 1996; Myers et al. 1997) and at 2.2 mm toward A2163 (Wilbanks et al. 1994).

Measurements near the Planck peak and on the Wien side are in principle more attractive, since (1) they allow the spectrum to be uniquely identified as SZ (as opposed to primordial CMB fluctuations), (2) the intensity enhancement relative to the Planck value is larger than the magnitude of the R-J decrement, (3) sources in the cluster are expected to give a negligible contribution at high frequency, and (4) they allow measurement of cluster peculiar velocities. Clearly, an unambiguous signature of its presence is provided by the simultaneous detections of the enhancement and the decrement.

Recently, Holzapfel et al. (1997) have reported the first detection at millimeter wavelengths of both the decrement and the enhancement of the effect toward A2163, while Lamarre et al. (1998) reported detections of the same cluster at 630 and 390 μm of the increment.

In this paper, we report a combined analysis of millimeter *ROSAT* and *ASCA* observations toward the *ROSAT* cluster RX J0658−5557, for which the simultaneous observations of the effect at 1.2 mm (positive) and at 2 mm (negative) were first reported elsewhere (Andreani et al. 1996a). The cluster was chosen because of its hot temperature ($T_e \sim 17$ keV), high X-ray luminosity [$L_x = (3.5 \pm 0.4) \times 10^{45}\ h_{50}^{-2}$ ergs s^{-1} in the range 0.1–2.4 keV] and large distance ($z = 0.31$); this last property is needed to cope with the Swedish ESO Submillimeter Telescope (SEST) beam size of 44″ on the sky (see below).

Sections 2 and 3 describe millimeter *ROSAT* and *ASCA* observations; the implications of these measurements for the evaluation of the Hubble constant are discussed in § 4. In § 5 we discuss the contamination from foreground and/or intracluster sources.

2. MILLIMETER OBSERVATIONS

2.1. *The Instrument*

A double-channel photometer was built and devoted to the simultaneous search for enhancement and decrement of the SZ effect. The system works simultaneously at 1.2 and 2 mm, using two bolometers cooled at 0.3 K by means of a ^{3}He refrigerator. The 2 mm band includes the peak brightness of the decrement in the SZ thermal effect, while the 1.2 mm bandwidth is a compromise between the maximum value of the enhancement in the SZ and the atmospheric transmission. The wavelength ranges are defined by two interference filters centered at 1.2 and 2 mm and cooled at 4.2 K, with bandwidths of 350 and 560 μm, respectively (response curves of the optical trains can be found in Pizzo et al. 1995 and in the Appendix). The collecting optics are made up of a dichroic mirror splitting the incoming radiation into two f/4.3 Winston cones cooled at 0.3 K, which define a field of view on the sky of 44″ at both frequencies. The beam separation on the sky was limited by the antenna chopping system and was set to the maximum chopping amplitude, 135″. The pointing accuracy was frequently checked and was always better then 3″–4″. Alignment of the two beams was accurately determined with calibrators and turned out to be better than 2″. We tested the quality of the beam shapes and measured the beam widths imaging the planets. Beam widths are reported in Table 1. Any deviation from a Gaussian surface turned out to be less than 1% (see Pizzo et al. 1995 for details).

This photometer was adapted to the focus of the SEST, and its performance was tested during an observing run in 1994 September. Details of the instrument can be found in Pizzo et al. (1995) and Andreani et al. (1996b); a brief description is also given in the Appendix.

2.2. *The Observations*

Responsivity measurements were conducted regularly during 1994 September and 1995 September by observing planets (Uranus, Saturn, Jupiter, Venus, and Mars), with Jupiter used as the primary calibrator. The main figures measured at the focus are listed in Table 1. The reported

TABLE 1

PERFORMANCES OF THE PHOTOMETER AT FOCUS

λ_c (μm)	$\Delta\lambda$ (μm)	FWHM (arcmin)	Noise (nV Hz$^{-1/2}$)	Responsivities (μV K^{-1})	NET$_{\rm ant}$ (mK s$^{-1/2}$)	$(\Delta T/T)_{\rm therm}$ (1 s)
1200.....	360	44	45	3.0	10.6	0.0142
2000.....	580	46	31	1.4	15.6	0.0099

NET is given in antenna temperature, while sensitivities are expressed as the relative change of the thermodynamic temperatures in a 1 s integration time (see Pizzo et al. 1995).

Calibration uncertainties are mainly related to uncertainties of the planet temperatures at millimeter wavelengths. We use the values quoted by Ulich (1981, 1984), who took measurements of the planets at the same frequencies. The uncertainties on the planet brightnesses quoted by this author are less than 10%. However, different measurements taken with our instrument during different nights of observations produce results that are sometimes off by more than 10%, because of changes in the observing conditions. Thus, we conservatively estimate that the final uncertainty on the antenna temperature is $\sim 15\%$.

A total integration time of 15,000 s was spent on the source during several different nights in 1995 September, and the same integration time was spent on blank sky located 15 minutes ahead in right ascension. Some of the data were discarded for the present work because they were corrupted by poor weather conditions. The remaining data are those collected during nights when the sky opacity was very low ($\tau_{1\ \mathrm{mm}} < 0.1$, with an average value of $\langle \tau_{1\ \mathrm{mm}} \rangle = 0.07$; $\tau_{2\ \mathrm{mm}} < 0.05$, with an average value of $\langle \tau_{2\ \mathrm{mm}} \rangle = 0.03$) and the sky emission very stable, thus producing a very low sky noise. The *effective* integration time was 12,000 s on-source.

In order to get rid of the major sources of noise in this kind of experiment—fluctuations in the atmospheric emission and systematics from the antenna—the observing strategy makes use of two combined procedures: the common three-beam technique, beam-switching + nodding, which gets rid of the linear spatial and temporal variations in the atmospheric emission, and observations of blank-sky regions located 15 minutes ahead in right ascension ($\Delta\alpha = 15$ minutes) with respect to the source. The latter implies that for each 10 minutes of integration on-source (10 minutes integration + overhead give a total tracking time of 15 minutes), a similar integration is performed on the blank sky. This level of switching corrects for offsets that are dependent on telescope orientation and related to diffracted radiation from the environment. The comparison between the two signals provides a measurement of the systematics introduced by the antenna. In fact, the instrument tracks the same sky position twice with respect to the local environment, once on-source and once on the blank sky. The choice of 600 s of integration on and off the source is a compromise between a minimization of the time wasted on overheads and the need to minimize the atmospheric variations between one observation and the next. In this way, the efficiency of the observations is not greatly reduced by frequent slewing, but is small enough that temporal variations are not too severe. Note that the sequence from on-source to off-source (on blank sky) was performed by the computer controlling the antenna and was therefore entirely automatic. The synchronization between the two measurements was as high as possible, with an estimated error of less than 2 s, negligible with respect to the beam size and integration step (10 minutes).

As the telescope tracks the cluster across the sky, the reference beams trace circular arcs around the cluster. The reference beams are always separated from the on-source position only in azimuth, and their positions are given in terms of parallactic angle p (the angle between the north celestial pole and the zenith):

$$\tan p = \frac{\cos \phi \sin H}{\sin \phi \cos \delta - \cos \phi \sin \delta \cos H},$$

where ϕ is the geographic latitude, and H and δ are the hour angle and the declination of the object, respectively. It would be better to have a wide distribution of parallactic angles to avoid contamination from sources in the reference beams. In Figure 6 we overplot the positions of the main and circular arcs swept by the reference beams on the SZ map obtained with the X-ray image (see below for details). Because of the complex X-ray map and the limited beam throw, which results in reference beams not being completely out of the X-ray emission, we need to carefully model the expected signal with this configuration before comparing theoretical expectations with the real data. This point is further discussed in § 4.

The data analysis procedure is described in detail in Andreani (1994) and Andreani et al. (1996b); here only the basic methods are described. The data consist of 200 s integration blocks (hereafter *one scan*), each containing 20 10 s subscans taken at two different antenna positions, A and B, with the reference beams on the left and right, respectively. The integration sequence was ABBAABBAABB...A. A second-order polynomial fit was subtracted from each scan in order to get rid of offsets in the electronics and large-scale atmospheric trends not completely cancelled out by the three-beam switching. Spikes caused by equipment malfunction were removed from each subscan (but the fraction of rejected data is less than 1%), and very high frequency atmospheric variations were smoothed with the Savitzky-Golay filter algorithm (Press & Teukolsky 1990). For each subscan, a mean value for the differential antenna temperature, T_A or T_B, is found by averaging over the 10 s. The variance, $\sigma^2_{A,B}$, is estimated with a procedure of bootstrap resampling (Barrow, Bhavsar, & Sonoda 1984). This method is widely used to take into account correlations among data (induced in this case by the filtering). The procedure requires for each subscan the creation of many mock subscans (in this case, 1000 for each), each containing the same number of data as the real one, created by randomly redistributing the data—i.e., the sequence numbers of the data are randomized. This means that in some cases one datum could be considered more than once, while in other cases it could be discarded. A mean value for the differential antenna temperature is then computed for each mock subscan. The bootstrap uncertainty for each real subscan is estimated by the standard deviation of the mean value of the 1000 mock subscans.

The signal is then obtained by subtracting each couple of subscans, $\Delta T_i = (T_A - T_B)/2$ with variance $\sigma_i^2 = (\sigma_A^2 + \sigma_B^2)/2$.

Weighted means are computed for each 200 s integration (1 scan) on each sky position (when the antenna tracks the source, ΔT_{ON}, and when the antenna tracks the blank sky, ΔT_{OFF}). Cluster signals are then estimated from the subtraction of each off-source from each on-source signal, $\Delta T_{\mathrm{SZ}} = \Delta T_{\mathrm{ON}} - \Delta T_{\mathrm{OFF}}$, and the quadratic sum of the two standard deviations are used to estimate errors: $\sigma^2_{\mathrm{SZ}} = \sigma^2_{\mathrm{ON}} + \sigma^2_{\mathrm{OFF}}$.

The lower panels of Figure 1 show these differences in antenna temperature as a function of time for both channels. The solid lines represent the maximum-likelihood estimates for ΔT_{SZ}, while the dotted lines show $\Delta T_{\mathrm{SZ}} \pm 3\,\sigma$.

The χ^2 tests, performed over the data reported in Figure 1, give values of $\chi^2 = 37.2$ and $\chi^2 = 34.2$ for 50 degrees of

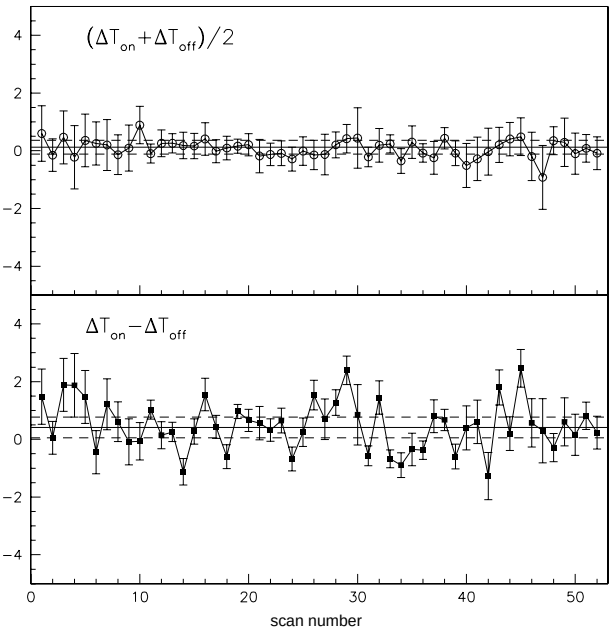

FIG. 1*a*

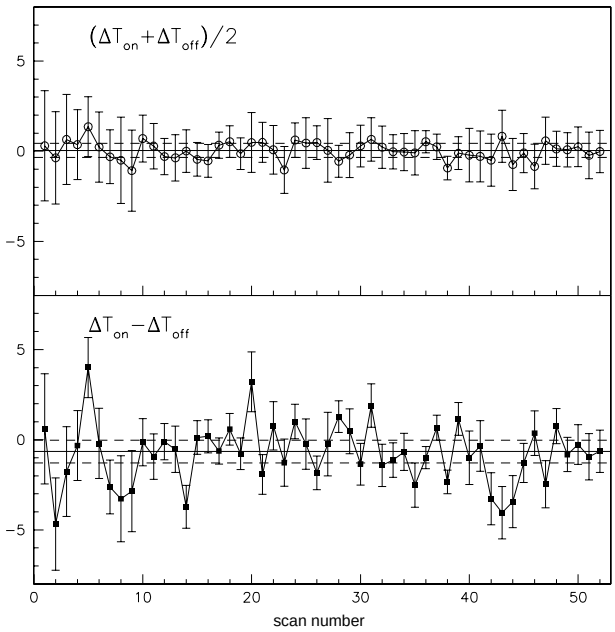

FIG. 1*b*

FIG. 1.—(*a*) Differential antenna temperatures at 1 mm for RX J0658−5557. The cluster signals are estimated by subtracting $\Delta T_{SZ} = \Delta T_{ON} - \Delta T_{OFF}$ and are reported in the lower panel. Upper panel shows the sum $(\Delta T_{ON} + \Delta T_{OFF})/2$, which is sensitive to any possible systematics. The maximum-likelihood values of ΔT_{SZ} are shown as solid lines; the dashed lines correspond to the $\pm 3\,\sigma$ confidence interval. (*b*) The same as *a*, but for the 2 mm channel.

freedom at 1 and 2 mm, respectively. From the maximum-likelihood estimates, we find $\Delta T_{1\,mm} = +0.30 \pm 0.07$ mK, $\Delta T_{2\,mm} = -0.50 \pm 0.15$ mK, where the uncertainties are given by the 70% confidence range. This was found by estimating the width of the likelihood curve corresponding to the values of the signal where the likelihood drops by a factor of 1.71 from its maximum. Maximum-likelihood curves are shown in Figure 2.

Converting these values to thermodynamic ones, we find 0.96 ± 0.22 mK at 1.2 mm and -0.86 ± 0.26 mK at 2 mm.

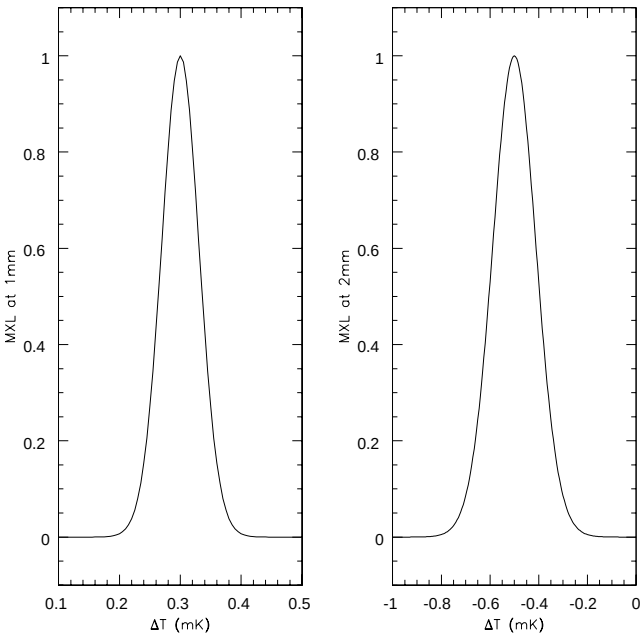

FIG. 2.—Maximum-likelihood curves of the data reported in Fig. 1. Abscissa values are in antenna temperatures.

The error bars associated with these values are only due to the statistics. To estimate those due to observing systematics, we have proceeded as follows.

To test any position-dependent systematics, Figure 1 also shows in the upper panels the sum $\Delta T_{sys} = (\Delta T_{ON} + \Delta T_{OFF})/2$. The statistics in these cases give weighted averages of 0.12 ± 0.08 mK at 1 mm and 0.04 ± 0.13 mK at 2 mm. The associated error bars will be quoted in the following discussion as systematic uncertainties, and will be considered in the final values of the Comptonization parameter (see § 4.3).

Another way to take the systematics into account is to estimate the error bars as in Andreani (1994) and Andreani et al. (1996b). For each ΔT_{SZ} a weight is assigned: $w_m = (\sigma_{SZ}^2 + \sigma_P^2)^{-1}$, where σ_{SZ}^2 represents the variance due to short-term fluctuations (those reported in Fig. 1 associated with each on-source/off-source difference), while σ_P^2 is the variance due to medium-term variations, i.e., related to any long-term systematics in these differences.

The final weighted mean is given by

$$\langle \Delta T_{SZ} \rangle = \frac{\sum_{m=1}^{N} \Delta T_{SZ}\, w_m}{\sum_{m=1}^{N} w_m}\,, \tag{3}$$

with estimated variance

$$\sigma_f^2 = \frac{1}{N-1} \frac{\sum_{m=1}^{N} (\Delta T_{SZ} - \langle \Delta T_{SZ} \rangle)^2 w_m}{\sum_{m=1}^{N} w_m}\,. \tag{4}$$

In this case, one finds 0.35 ± 0.11 and -0.61 ± 0.20 mK (antenna temperature) at 1 and 2 mm, respectively. The error bars here are equal to the quadratic sum of the error bars due to statistics and systematics, estimated above.

In order to check whether the detections are spurious, caused by the equipment (microphonics and slewing of the telescope), we have carried out additional measurements while blocking off the beam; an aluminum sheet was put on

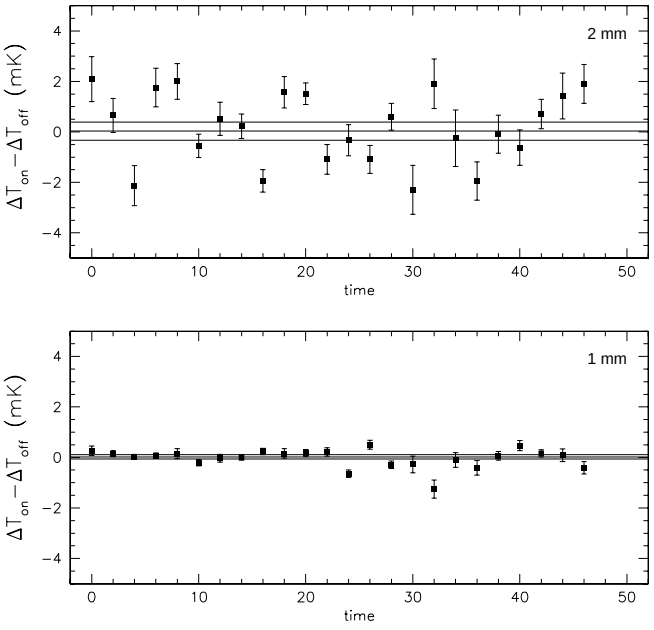

FIG. 3.—Antenna temperature differences, $\Delta T_{ON} - \Delta T_{OFF}$, taken with the photometer window covered with a metal sheet. The same observing procedure on and off the source was applied with this configuration to test the photometer systematics. It is clear that there are no spurious signals generated from the instrument. Solid lines correspond to the averages computed over the plotted data $\pm 3\,\sigma$. Note that the total integration time in this case is 3 times shorter than that in Fig. 1.

the entrance window of the photometer, located so as to cover the entire window and prevent diffracted radiation from entering the photometer. The same double blank-sky observing sequence on and off the source, i.e., the same alto-azimuthal paths, were tracked with this configuration for 5000 s; the resulting signals are shown in Figure 3.

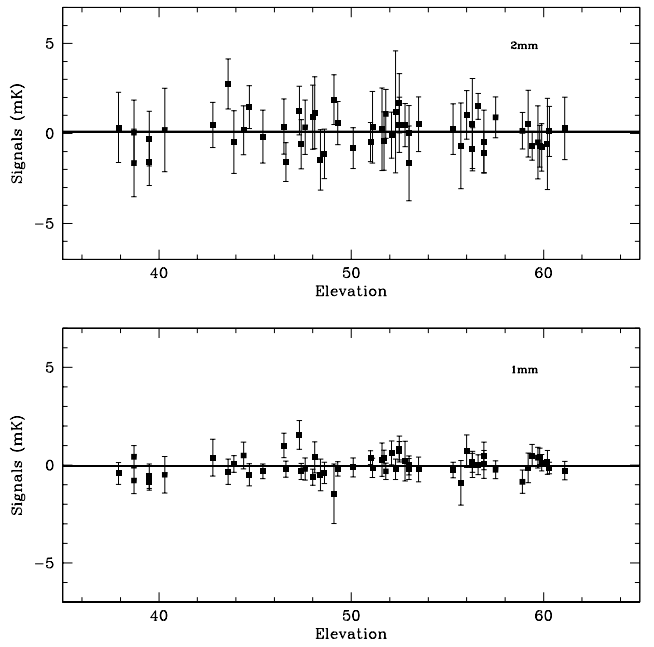

FIG. 4.—Antenna temperature values taken off the source (on a blank sky at a position 15 minutes ahead in R.A.) as a function of the elevation of the source. Solid lines correspond to the averages in antenna temperatures, 0.09 ± 0.06 mK (2 mm, *top*) and -0.03 ± 0.02 mK (1 mm, *bottom*)

No signals are detected with the window covered by the metal sheet, and there is no trend in the signal as a function of the alto-azimuthal position. We conclude that there are no systematics coming from the photometer; the two channels behave properly and do not introduce spurious signals. The rms values of the signals stored with the window covered by the metal sheet turn out to be 0.07 and 0.15 mK (antenna temperatures) at 1 and 2 mm, respectively. These values can be used as an estimate of the instrumental noise during the observations, once they are scaled to the integration time spent on the source: 0.05 and 0.1 mK (antenna temperatures) at 1 and 2 mm, respectively. This does not mean that this procedure takes into account all the antenna systematics when the photometer looked at the source and the blank sky. Some spurious signals may survive if the antenna did not precisely track the same paths relative to the local environment because of a loss of synchronization. As already reported above, we have tried to quantify the error in the position of the hour-angle track for the off position, i.e., the error in synchronization, and we estimate that it is 2 s, which is much lower than the beam size and the nodding interval of 10 s.

A further check on environmental systematics that could affect the SZ signals was performed by investigating any dependence of blank-sky signals on elevation. Figure 4 shows the signals recorded with the antenna pointed at the blank sky as a function of the elevation. There is no evident systematics affecting the observations.

3. *ROSAT* AND *ASCA* OBSERVATIONS

Details of *ROSAT* and *ASCA* observations of this source can be found in Böhringer & Tanaka (1997). Here we briefly summarize the main X-ray properties.

3.1. *ROSAT Data*

The galaxy cluster RX J0658−5557 was independently discovered in the *Einstein* slew survey (Tucker, Tananbaum, & Remillard 1995) as the source 1E 0657−55, and in a follow-up identification program for galaxy clusters in the *ROSAT* All Sky Survey (RASS) at ESO started in 1992 (Böhringer 1994; Guzzo et al. 1995) as X-ray source RX J0658.5−5557. The cluster is extremely X-ray bright, and was therefore scheduled for various follow-up observations with *ROSAT*, *ASCA*, and optical spectroscopy measurements.

RX J0658−5557 was detected in the RASS with a count rate of 0.5 ± 0.04 counts s^{-1} in the 0.1–2.4 keV band and 0.41 ± 0.04 counts s^{-1} in 0.5–2 keV, which corresponds to a 0.1–2.4 keV flux of $(8.5 \pm 0.9) \times 10^{-12}$ ergs s^{-1} cm^{-2} and an X-ray luminosity of $L_X = (3.50 \pm 0.40) \times 10^{45}\ h_{50}^{-2}$ ergs s^{-1} (0.1–2.4 keV). For the luminosity calculation, we used a value of 17 keV for the temperature, $N_H = 3.5 \times 10^{20}$ cm^{-2} for the absorbing column density, and a metallicity of 0.35 of the solar value, parameters inferred from the *ASCA* spectral analysis (see below). The cluster was also observed in a pointed observation with the *ROSAT* HRI (P.I.: W. H. Tucker) for 58 220 s and was detected with a count rate of (0.166 ± 0.005) counts s^{-1}, yielding an X-ray luminosity of $L_X = (3.44 \pm 0.15) \times 10^{45}\ h_{50}^{-2}$ ergs s^{-1} in the rest-frame 0.1–2.4 keV energy band, in very good agreement with the PSPC data.

The *ROSAT* band flux calculated from the HRI observation is $(8.3 \pm 0.3) \times 10^{-12}$ ergs s^{-1} cm^{-2}. We also made use of a *ROSAT* PSPC observation conducted in 1997

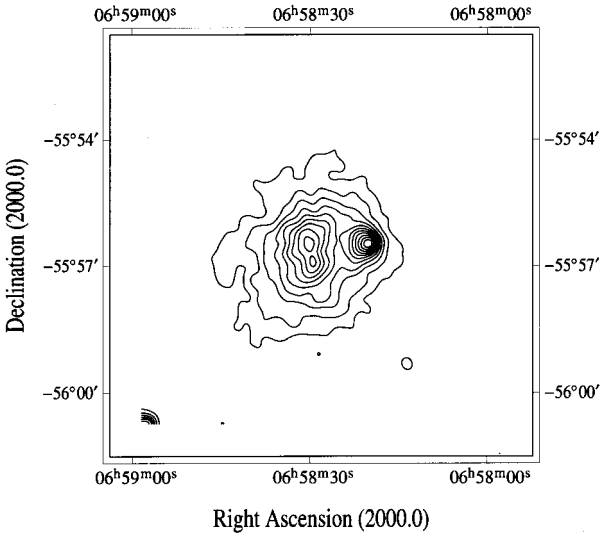

FIG. 5.—X-ray image of the RX J0658−5557 cluster observed with the *ROSAT*/PSPC. The contour levels are logarithmically spaced, with the peak brightness corresponding to 9.4×10^{-2} counts arcmin^{-2}.

February, with an exposure of about 5 ks, in order to check the astrometry.

Figure 5 shows the *ROSAT* HRI image of the cluster: the X-ray morphology is quite complex, the cluster center being dominated by two blobs, with the western component (hereafter component 2) less luminous. This may indicate a merging process in the two substructures, a morphology that complicates the modeling of the X-ray surface brightness as discussed in § 4.

3.2. *ASCA Observations*

RX J0658−5557 was observed with *ASCA* on 1996 May 10 for a total observing time of ~40 ks. A peak at around 5 keV is conspicuous due to the redshifted iron *K*-lines, from which the redshift parameter can be determined. The Raymond-Smith model was employed for fitting model spectra to the observed data. The best-fit results obtained from the GIS spectrum are $kT = 17.0 \pm 4.0$ keV, the abundance of elements is 0.35 ± 0.13 of the solar abundance, the redshift is $z = 0.31 \pm 0.03$, and the absorption column is $N_{\rm H} \leq 6 \times 10^{20}$ cm^{-2}. The errors are at the 90% confidence level. The redshift of the cluster was also confirmed by optical spectroscopy of eight galaxy members (data are published in Tucker et al. 1998).

The observed flux in the 2–10 keV range is approximately 0.9×10^{-12} ergs s^{-1} cm^{-2}, from which the total bolometric flux is estimated to be $\sim 2 \times 10^{-11}$ ergs s^{-1} cm^{-2}. For $z = 0.31$, the bolometric luminosity is $\sim 1.1 \times 10^{46}$ ergs s^{-1}. Thus, RX J0658.5−5557 is one of the hottest and most luminous clusters known to date, and so is ideal for observations of the SZ effect.

The accuracy of the absolute calibration of the two satellites is difficult to assess. Cross-calibrations among the different instruments agree to within a factor of 10%.

4. MODELING THE HUBBLE CONSTANT

The angular diameter distance to a cluster can be observationally determined by combining measurements of the thermal SZ effect and X-ray measurements of thermal emission from intracluster (IC) gas. Thus, the value of H_0 can be deduced from these measurements, as many authors have discussed in the past (Cavaliere, Danese, & DeZotti 1979; Birkinshaw, Hughes, & Arnaud 1991; Holzapfel et al. 1997; Myers et al. 1997).

4.1. *Modeling the X-Ray Data*

Unfortunately, this cluster has a complex morphology, making it difficult to use a simple geometrical model to fit the surface brightness. There is no unique way to deproject the X-ray surface brightness distribution to derive the volume emissivity and the electron density distribution. A pragmatic approach is to model the cluster with two symmetrical components centered at the two X-ray maxima. While the smaller western component (2) is quite round and compact, the eastern one (component 1) appears elongated in the north-south direction in the central region. At large radii, however, the cluster becomes more azimuthally symmetrical. Thus, a spherically symmetrical model also provides a fair average approximation of the slightly elongated structure as shown by, e.g., Neumann & Böhringer (1997). We then fit empirical β models to the azimuthally averaged surface-brightness profiles and compute through an analytical deprojection the distribution of the IC gas column density along the line of sight (Cavaliere & Fusco-Femiano 1976):

$$n(\theta) \propto \left(1 + \frac{\theta^2}{\theta_c^2}\right)^{-(3/2)\beta + 1/2}, \qquad (5)$$

in which β and the cluster angular core radius (θ_c) are left as free parameters. We performed the actual fits to the profiles of the undistorted side of component 1 and the less distorted western side of component 2 in the high-resolution *ROSAT*/HRI data. The resulting parameters of the two best-fit models are listed in Table 2.

The electron densities corresponding to these surface brightness values are 6.3×10^{-3} and 1.5×10^{-2} cm^{-3} for the western and eastern components, respectively ($H_0 = 50$ km s^{-1} Mpc^{-1} was used in this calculation).

The X-ray observations were then used to make a prediction for the expected SZ increment or decrement. The numerical values in this calculation depend on the Hubble parameter, H_0, and in this way, by comparing the predicted with the measured values, an estimate of the absolute distance of the cluster and H_0 can be made.

TABLE 2

RESULTS OF THE β MODEL FITS TO THE SURFACE BRIGHTNESS PROFILES OF THE *ROSAT* PSPC AND HRI OBSERVATIONS

Data	S_0 (counts s^{-1} arcmin^{-2})	Core Radius (arcmin)	β	r_c (h_{50}^{-1} Mpc)
Eastern component	0.027	1.23	0.7	0.406
Western component.....	0.046	0.26	0.49	0.086

The first step was to compute the Comptonization parameter, Y, for the models given in the previous subsection. The parameter Y at the cluster center is given by

$$Y = \frac{kT_e\sigma_\tau}{m_e c^2}\int_{-R}^{+R} n_e(r)\,dr \quad h_{50}^{-1/2}\,, \tag{6}$$

where R is the outer radius of the cluster. We took the estimated virial radius as $3\,h_{50}^{-1}$ Mpc.

Since we do not have spatially resolved information on the temperature distribution, the thermal structure of the IC gas is also assumed to be radially symmetrical and isothermal. One effect of deviations from isothermality is discussed below.

Numerically, a β-modeled cluster has a Comptonization parameter

$$Y = 1.3\times 10^{-27}\ \mathrm{cm}^2\left(\frac{T_e}{1\ \mathrm{keV}}\right)n_e(0)r_c \times\left[\frac{\sqrt{\pi}\Gamma(1.5\beta-0.5)}{\Gamma(1.5\beta)}\right]h_{50}^{-1/2}\,, \tag{7}$$

where $n_e(0)$ is the central electron density and r_c is the core radius of the cluster plasma halo. The last equation is not *formally* consistent with equation (6), because in this case the integration limit is infinite, while in the former equation the integration is performed up to the virial radius. The error on the Y parameter introduced by choosing a wrong (because unknown) outer radius is estimated to be small (less than 5%).

Inserting the values listed in Table 2, we find the following Y-parameters at the center of each component:

$$Y = 4.90\times 10^{-4}\ h_{50}^{-1/2} \quad \text{for component 1}\,, \tag{8}$$

$$Y = 4.80\times 10^{-4}\ h_{50}^{-1/2} \quad \text{for component 2}\,. \tag{9}$$

To compare the predicted SZ effect values with those obtained from the observations, the Y-parameter at the position of the observations in the composite model must be evaluated. Since the observed SZ signal is the true one modified by the telescope primary beam and the beam switching, the predicted Y-parameter must be convolved with beam pattern and throw. We can well approximate the beam pattern with a Gaussian (Pizzo et al. 1995):

$$G(\alpha) = \frac{1}{2\pi\sigma^2}\exp\left(-\frac{\alpha^2}{2\sigma^2}\right), \tag{10}$$

where σ is roughly half the beam width (44″/2.3), and the average signal in the Gaussian beam is

$$\tilde{Y}(\rho) = 2\pi\int \rho' d\rho'\,\frac{1}{2\pi L^2}\exp\left(\frac{-\rho'^2}{2L^2}\right)Y(\rho')\,, \tag{11}$$

where $L = D_a\,\sigma$, and ρ is the angular radius from the cluster center. Once ρ is expressed in terms of right ascension and declination, the integral becomes a double integral.

The beam switching introduces a gradient with the value

$$\langle\Delta Y_{\mathrm{sw}}\rangle = \tilde{Y}(0) - \frac{1}{2}\,\tilde{Y}(R_-) - \frac{1}{2}\,\tilde{Y}(R_+)\,, \tag{12}$$

where $R_\pm$ corresponds to the two positions of the reference beams at a distance from the center $D = D_a\,\theta_D$, where $\theta_D = 135''$ is the beam separation.

To compare the measured values with the expected signals from the cluster, we first convolved the predicted SZ surface brightness from the X-ray model using a two-dimensional filtering (eq. [11]), and then averaged the Y-values over the positions of the projected reference beams in the northwestern and southeastern arcs, whose average centers are given by the coordinates (J2000) 104.°6665, −55.°9231 (northern offset) and 104.°6063, −55.°9865 (southern offset). The central beam position is 104.°6363, −55.°9551. The resulting values are

$$\begin{aligned} &6.4\times 10^{-4}\ \text{(center)}\,,\\ &4.0\times 10^{-4}\ \text{(north), and}\\ &3.3\times 10^{-4}\ \text{(south)}\,. \end{aligned} \tag{13}$$

The averaged ΔY-parameter is $\Delta Y = 2.70\times 10^{-4}$.

At this point, it is very important to investigate the influence of the pointing accuracy on the results. On the one hand, there is the uncertainty on the pointing offset of the telescope (discussed in § 2); on the other hand, there are the uncertainties related to the PSPC and HRI pointings. While we can safely assume that the *relative* pointing accuracy of SEST is better than 3″, recovering the astrometry of the PSPC image was not an easy task because of the uncertainties in the positions of the known sources in the field.

The PSPC and HRI pointings agree to within 10″. Therefore, we allow an overall pointing accuracy of about 20″. This in turn reflects into an uncertainty on the estimated ΔY.

Figure 6 shows the convolved SZ surface brightness predicted with the X-ray model described above. Superimposed are the northern and southern arcs of the reference beams (*crosses*) and the position of the main beam (*open square*).

We see that the combination of the beam size and the limited chop throw has the effect that the Comptonization parameter has about half of the central value at the offset reference positions.

4.2. *Errors on Y from X-Ray Modeling*

A critical point in these results is the uncertainty on the idealized model of the cluster plasma halo. In particular, the merging configuration, indicated by the high-resolution X-ray image of the cluster, does not allow for correct modeling. There is, however, a clear indication in the X-ray images that the main component is quite extended and almost symmetric at large radii, while the smaller component appears bright as a result of its high central density, but is quite compact. We can therefore conclude that the main component carries a very large fraction of the gas mass and total mass, and that it is only slightly disturbed on a global scale by the merging smaller and more compact group. We expect that the major contribution to the SZ signal comes by far from the main component, and that the small infalling cluster makes only a minor contribution. The strategy of measuring the SZ signal slightly off the peak at the opposite side of the merger further decreases the influence of the infalling clump.

Thus, a pragmatic approach to estimating the uncertainty of the result for the Comptonization parameter is to explore several alternatives, preferably extreme models, which should help to bracket the true result.

1. The first alternative model considers only the halo of component (1) to calculate the expected value for the Com-

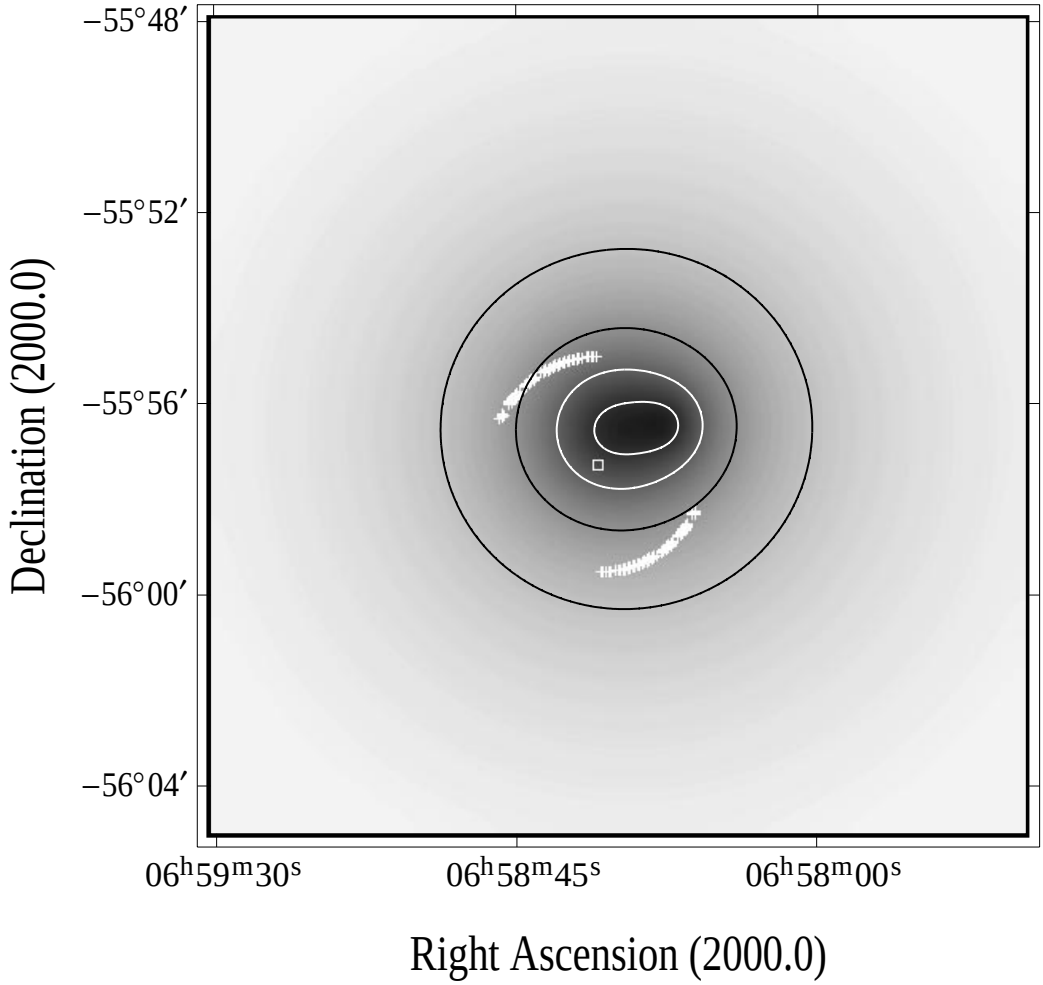

FIG. 6.—Convolved SZ surface brightness predicted with the X-ray model described in § 4.1. Superimposed are the northern and southern arcs of the reference beams (*lines of crosses*) and the position of the main beam (*open square*).

ptonization parameter. It turns out that in this scenario, $\Delta Y = 2.2 \times 10^{-4}$. The justification for this model is that the smaller component may actually have a much smaller T_e than the main component, and/or it may not be as extended as assumed in our model. In both cases, the effect of this component would be considerably overestimated. Thus, by completely neglecting this latter component, the resulting Y-value is a lower limit to the real one.

2. We then compute another alternative model, changing the temperature profile from the isothermal case. If there is a temperature gradient that decreases with radius, the Y image will be more compact, at variance with what we found using the second model. The easiest analytical model for a temperature gradient is a polytropic model with

$$\frac{T(r)}{T_0} = \left[\frac{n(r)}{n_0}\right]^{\gamma - 1}, \qquad (14)$$

where γ is the polytropic index. If we assume a quite large value of $\gamma = 1.4$, we find $\Delta Y = 2.10 \times 10^{-4}$. The resulting difference in Y is on the one hand enhanced by the greater compactness of the cluster, and on the other hand shrunken because of the decrease of the central value, Y_0.

Comparing the results of the various models, we quote as a conservative uncertainty a factor of 1.3 in the parameter ΔY. Since H_0 depends quadratically on this value (eq. [4]), the uncertainty in the final estimate of H_0 is roughly a factor of 1.6.

The uncertainty in the overall temperature measurement is less than 4 keV at the 2 σ limit, and introduces an error of 25%.

Another aspect of the structure of the intracluster plasma that introduces uncertainties is the possible clumpiness of this medium. This effect was, for example, considered by Birkinshaw (1991) and Holzapfel et al. (1997) and investigated by means of simulations by Inagaki, Suginohara, & Suto (1995) and Roettiger, Stone, & Mushotzky (1997). For reasonable clumping scenarios, a clumpy medium has the effect of lowering the H_0 value by about 10%–20%. No direct evidence for a clumpy intracluster medium was found, however, and the models suggested, as well as the following estimated uncertainty, are still highly speculative.

We then consider 65% as a conservative uncertainty on the estimate of the Hubble constant quoted below, derived only from modeling.

4.3. *Modeling* H_0

The conversion of the Comptonization parameter to the observed change in antenna temperature is given by equations (1) and (2), whose right-hand sides must be integrated over the instrumental bandwidths. Following Challinor &

Lasenby (1998), we integrate over the instrument bandwidths equation (2), which takes into account the relativistic corrections, and find

$$\left(\frac{\Delta T}{T}\right)_{1.2\ \mathrm{mm}} = 0.38Y\ , \tag{15}$$

$$\left(\frac{\Delta T}{T}\right)_{2\ \mathrm{mm}} = -1.20Y\ . \tag{16}$$

Hence, the predicted versus observed changes are

$$\left(\frac{\Delta T}{T}\right)_{\text{X-ray}} = 1.03 \times 10^{-4}\ h_{50}^{-1/2}\ ,$$

$$\left(\frac{\Delta T}{T}\right)_{\text{obs}} = 3.3 \times 10^{-4} \tag{17}$$

for the 1.2 mm channel, giving a formal result for the Hubble constant of $H_0 = 5$ km s^{-1} Mpc^{-1}. For the 2 mm channel, one finds

$$\left(\frac{\Delta T}{T}\right)_{\text{X-ray}} = -3.24 \times 10^{-4}\ h_{50}^{-1/2}\ ,$$

$$\left(\frac{\Delta T}{T}\right)_{\text{obs}} = -3.16 \times 10^{-4}\ , \tag{18}$$

giving a formal result for the Hubble constant of $H_0 = 53^{+38}_{-28}$ km s^{-1} Mpc^{-1}. The error bars take into account the uncertainties on the pointing position of the SEST and *ROSAT* telescopes, on the X-ray modeling (as discussed in § 4.2), and on the millimeter observations (both statistics and systematics).

5. ORIGIN OF THE DETECTED SIGNALS

In the following section, we discuss the possible contamination of the observed signals by spurious sources. Radio sources would more affect the 2 mm signal, thermal sources the 1.2 mm signal.

Let us assume for the moment that the decrement seen at 2 mm (eq. [16]) is due to the thermal SZ effect. From this value, the *expected* 1 mm signal can be easily computed from equation (2). Comparing this with the value derived from the observations (eq. [15]), a difference of a factor of 3 is found; the reason for this discrepancy was investigated in several ways, as discussed below.

On the other hand, if we consider the 1 mm signal as only due to the thermal SZ effect, the expected absolute 2 mm value would be higher by a factor of 3. In this case, it is straightforward to check whether any radio source is present in the main beam.

5.1. *Possible Source Contamination*

The presence of a source contaminating the signals was checked as shown below. We then first assume that a thermal source is present in the main beam, giving rise to a signal of 0.3 mK in antenna temperature. A thermal source is stronger at 1.2 mm than at 2 mm by a factor of roughly $(2/1.2)^{3.5}$ (Andreani & Franceschini (1996c)), and therefore it would be a factor of 6 weaker at 2 mm; the expected signal in the 2 mm channel would be only 0.05 mK, well within the error bars. We then checked the likely presence of such a source in the cluster center, with these results:

1. No sources in the *IRAS* Faint Source Catalogue are present at the position of the main beam and/or the reference beams.

2. If we scale the 60 μm *IRAS* flux limit of 240 mJy at 1.2 mm by using the average flux of nearby spirals (Andreani & Franceschini 1996c), we find that a normal spiral would give rise to a signal not larger than 0.02 mK in antenna temperature. Therefore, it should be a peculiar galaxy.

3. If we assume a contribution from many unresolved sources fluctuating in the beam and take the estimation made by Franceschini et al. (1991), the expected signal will be not larger than 0.02 mK.

4. Irregular emission from Galactic cirrus can also give rise to a signal at these wavelengths. If we take the estimation by Gautier et al. (1992) and extrapolate the 100 μm flux at 1.2 mm using the average Galactic spectrum, a maximum signal of 0.02 mK is found.

5. The 60 and 100 μm emission from a handful of nearby clusters detected by *IRAS* has been interpreted as evidence for cold dust in the ICM (Stickel et al. 1997; Bregman & Cox 1997). Dust grains hardly survive in the ICM, and their lifetime would be very short in these environments; thus, the probability of detection is very low. This does not exclude the presence of dust in RX J0658−5557 that would more strongly affect the 1.2 mm channel.

6. Let us now consider the case of radio-source contamination. In general, radio sources have spectra that decrease with increasing frequency; thus, the effects of radio-source contamination at 1.2 and 2 mm are greatly reduced compared to observations at radio frequencies. However, there are radio sources with spectra that rise with frequency. Radio maps of the cluster were obtained with the Australia Telescope at 8.8, 5, 2.2, and 1.3 GHz. The sources in the 8.8 GHz image were weaker than 10 mJy (after primary-beam correction), and all the sources within the primary beam ($\sim 3'$ radius) had spectra that decrease with increasing frequency. A radio halo source the size of the X-ray emission was found to coincide with the X-ray emission with a total flux of ~ 3 mJy at 8.8 GHz and a spectral index of -1.7. The contamination to the main beam is $\ll 0.001$ mK at both 1.2 and 2 mm, and thus negligible. The reference beams are not contaminated by the radio sources. Details of the properties of the radio sources in the field will be the subject of another paper (Liang et al., in preparation).

We conclude that it is possible that part of the signal at 1.2 mm is due to diffuse emission from an eventual intracluster dust; this point deserves further investigation and is the goal of future research (for instance, *ISO* mapping at 200 μm).

5.2. *CMB Anisotropies and Peculiar Velocity*

Peculiar velocities of a cluster could alter the thermal SZ effect by a factor of $(v_r/c)\tau$ (where τ is the optical depth through the halo gas). τ was estimated from the X-ray measurements, and turns out to be $\tau = 39Y$. If the cluster recedes from us with a velocity of 1000 km s^{-1}, the 1.2 mm signal would be enhanced only by 10%, and will therefore still be incompatible with the 2 mm signal. Values for the peculiar velocity larger than these are not found in optical searches, and seem to be excluded in most cosmological models.

If part of the signal is due to CMB anisotropies at these scales, it will be hard to disentangle them from the SZ kinematic effect, since the latter has a spectrum identical to that

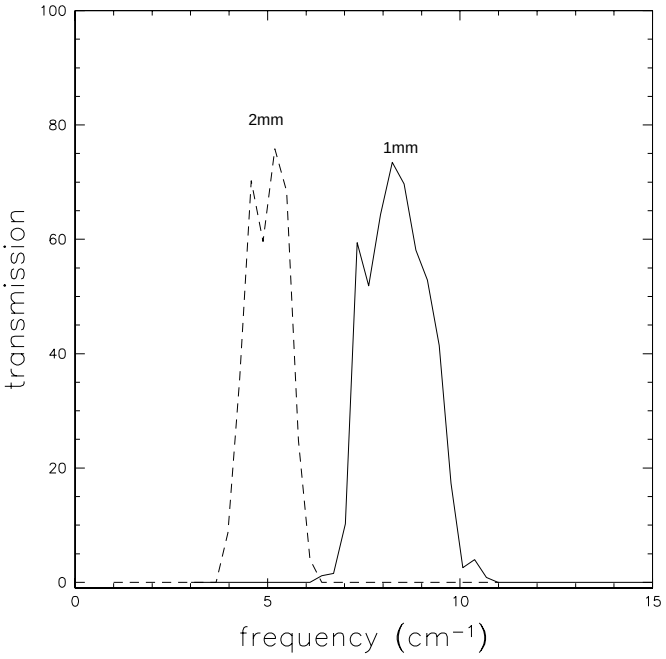

FIG. 7.—Transmission spectra of the two optical trains defining the wavelength ranges of the two channels at 1 mm ($\sim$8.5 cm^{-1}) and 2 mm ($\sim$5 cm^{-1}).

of the anisotropies (see, e.g., Haehnelt & Tegmark 1996). However, CMB anisotropies originating at redshifts larger than that of the cluster can be amplified by the gravitational lensing effect of the cluster itself, and so can affect the signal quite significantly (see Cen 1998).

CMB anisotropies will enhance both signals equally, thus reducing the amplitude of the 2 mm decrement. This means that the real 2 mm signal due to the SZ thermal effect alone would be larger, and the difference between the 1 and 2 mm values would shrink.

6. CONCLUSIONS

Observations at millimeter wavelengths of the Sunyaev-Zeldovich effect toward the X-ray cluster RX J0658$-$5557 were performed with the SEST telescope at La Silla (Chile), equipped with a double-channel photometer.

The observations were compared with models of the expected SZ effect computed on the basis of X-ray *ROSAT* and *ASCA* data for the source.

From the detected decrement, we infer a Comptonization parameter of $(2.60 \pm 0.79) \times 10^{-4}$, which is consistent with that computed using the X-ray images. The 1.2 mm channel data alone gives rise to a larger Comptonization parameter, and this result seems to be unexplained by the presence of known sources in the cluster, unless a strong emission from intracluster dust is found. Unknown instrument systematics could also contribute to this discrepancy.

We then use *ROSAT* and *ASCA* X-ray observations to model the SZ surface brightness. Since the cluster is asymmetrical and probably in a merging process, modeling is only approximate. The complex morphology of the cluster has been taken into account by exploring a set of alternative models, which were used to bracket the associated uncertainty. We then find as the global uncertainty on the Comptonization parameter a factor of 1.3.

We have also considered the effects of the pointing uncertainties of the *ROSAT* and SEST telescopes on the estimated Y.

The combination of the SZ and the X-ray measurements allows us to estimate a value for the Hubble constant: $H_0(q_0 = \frac{1}{2}) = 53^{+38}_{-28}$ km s^{-1} Mpc^{-1}, where the uncertainty is conservative and takes into account the uncertainties related to modeling the X-ray plasma halo, the pointing accuracy, and the statistical/calibration/systematics uncertainty of the millimeter observations.

As a final exercise, we determine the total gas mass from the SZ measurements and compare it with that inferred from the X-ray data. Following Aghanim et al. (1997), we find, for $H_0 = 50$ km s^{-1} Mpc^{-1} ($q_0 = 0.5$),

$$M_{\rm gas/SZ} = \frac{(\sqrt{1+z}-1)^2}{(1+z)^3}\,\frac{Y}{0.43}\left(\frac{10\ {\rm keV}}{kT_e}\right)h^{-2} \times 10^{14}\ M_\odot$$
$$= 3.15 \times 10^{15}\ M_\odot\ ,$$

where Y is the integral over the solid angle of the Comptonization parameter $Y = \int (y d\Omega)/(10^{-4}\ {\rm arcmin}^2)$.

The ratio $M_{\rm gas/X\text{-}ray}/M_{\rm gas/SZ} = 1.11\ h_{50}^{-1/2}$ is derived by integrating the mass of the X-ray–emitting gas using the hydrostatic isothermal β model with the parameters given in Table 2 up to the virial radius ($3\ h_{50}^{-1}$ Mpc). The agreement between the two estimates is excellent, within the large error bars, for $H_0 = 50$ km s^{-1} Mpc^{-1}.

The authors are indebted to the ESO/SEST teams at La Silla and in particular to Peter de Bruin, Peter Sinclair, Nicolas Haddad, and Cathy Horellou. This work has been partially supported by the P.N.R.A. (Programma Nazionale di Ricerche in Antartide). P. A. warmly thanks ESO for hospitality during 1995, when part of this work was carried out. We thank Yasushi Ikebe for his help in the reduction of the *ASCA* data. We are grateful to the editor, E. L. Wright, and to an unknown referee, whose suggestions and comments helped in improving the paper. We made use of the *Skyview* Database, developed under NASA ADP Grant NAS5-32068.

APPENDIX

A BRIEF DESCRIPTION OF THE PHOTOMETER

The photometer is a two-channel device covering the frequency bands 129–167 GHz and 217–284 GHz. It uses two Si bolometers cooled to 0.3 K by means of a single-stage ^{3}He refrigerator. Radiation coming from the telescope is focused by a PTFE lens and enters the cryostat through a polyethylene vacuum window and two Yoshinaga edge filters, one cooled at 77 K and the other cooled at 4.2 K. A dichroic mirror (a low-pass edge filter/beam splitter) at 4.2 K divides the incoming radiation between two f/4.3 Winston cones cooled at 0.3 K located orthogonal to each other.

A1. OPTICS RESPONSE

The wavelength ranges are defined by two interference filters centered at 1.2 and 2 mm, cooled at 4.2 K, with bandwidths of 350 and 560 μm, respectively. Their rejection factor has been estimated to be better than 10^{-6}. At the Winston cone entrance, a further Yoshinaga-type filter cooled at 0.3 K is installed. Figure 7 shows the measured transmission spectra of the two trains of filters from the vacuum window to the final Yoshinaga at 0.3 K.

REFERENCES

Aghanim, N., De Luca, A., Bouchet, F. R., Gispert, R., & Puget, J. L. 1997, preprint (astro-ph/9705092)
Andreani, P. 1994, ApJ, 428, 447
Andreani, P., et al. 1996a, in Proc. XVIth Moriond Astrophysics Meeting, Microwave Background Anisotropies, ed. F. R. Bouchet, R. Gispert, & B. Guiderdoni (Gif-sur-Yvette: Editions Frontières), 371
———. 1996b, ApJ, 459, L49
Andreani, P., & Franceschini, A. 1996c, MNRAS, 283, 85
Barrow, J. D., Bhavsar, S. P., & Sonoda, D. H. 1984, MNRAS, 210, 19
Birkinshaw, M. 1991, in Physical Cosmology, ed. A. Blanchard et al. (Gif-sur-Yvette: Editions Frontières), 177
———. 1997, Phys. Rep., in press
Birkinshaw, M., & Gull, S. F. 1984, MNRAS, 206, 359
Birkinshaw, M., Hughes, J. P., & Arnaud, K. A. 1991, ApJ, 379, 466
Bregman, J. N., & Cox, C. V. 1997, preprint (astro-ph/9712171)
Böhringer, H. 1994, in MPE Rept. 256, Studying the Universe with Clusters of Galaxies, ed. H. Böhringer & S. C. Schindler (Munich: MPE), 93
Böhringer, H., & Tanaka, Y. 1997, in preparation
Carlstrom, J. E., Joy, M., & Grego, L. 1996, ApJ, 456, L75
Cavaliere, A., Danese, L., & DeZotti, G. 1979, A&A, 75, 322
Cavaliere, A., & Fusco-Femiano, R. 1976, A&A, 49, 137
Cen, R. 1998, ApJ, 498, L99
Challinor, A., & Lasenby, A. 1998, ApJ, 499, 1
Franceschini, A., et al. 1991, A&AS, 89, 285
Gautier, T. N., Boulanger, F., Perault, M., & Puget, J. L. 1992, AJ, 103, 1313
Grainge, K., et al. 1993, MNRAS, 265, L57
Guzzo, L., et al. 1995, in Wide-Field Spectroscopy and the Distant Universe, ed. S. J. Maddox & A. Aragón-Salamanca (Singapore: World Scientific), 205
Haehnelt, M. G., & Tegmark, M. 1996, MNRAS, 279, 545
Herbig, T., Lawrence, C. R., Readhead, A. C. S., & Gulkis, S. 1995, ApJ, 449, L5
Holzapfel, W. L., Ade, P. A. R., Church, S. E., Mauskopf, P. D., Rephaeli, Y., Wilbanks, T. M., & Lange, A. E. 1997, ApJ, 480, 449
Inagaki, Y., Suginohara, T., & Suto, Y. 1995, PSAJ, 47, 411
Jones, M., et al. 1993, Nature, 365, 320
Klein, U., Rephaeli, Y., Schlickeiser, R., & Wielebinski, R. 1991, A&A, 244, 43
Lemarre, J. M., et al. 1998, ApJ, 507, L5
Myers, S. T., Baker, J. E., Readhead, A. C. S., Leitch E. M., & Herbig, T. 1997, ApJ, 485, 1
Neumann, D., & Böhringer, H. 1997, MNRAS, 289, 123
Pizzo, L., Andreani, P., Dall'Oglio, G., Lemke, R., Otàrola, A., & Whyborn, N. 1995, Exp. Astron., 6, 249
Press, W. H., & Teukolsky, S. A. 1990, Computers in Phys., 4, 669
Rephaeli, Y. 1995a, ARA&A, 33, 541
———. 1995b, ApJ, 445, 33
Roettiger, K., Stone, J. M., & Mushotzky, R. F. 1997, ApJ, 482, 588
Stickel, M., Lemke, D., Mattila, K., Haikala, L. K., & Haas, M. 1997, A&A, in press
Sunyaev, R. A., & Zeldovich, Ya. B. 1972, Comments Astrophys. Space Phys., 4, 173
———. 1981, Ap&SS, 1, 11
———. 1980, MNRAS, 190, 413
Tucker, W. H., Tananbaum, H., & Remillard, R. A. 1995, ApJ, 444, 532
Tucker, W. H., et al. 1998, ApJ, 496, L5
Ulich, B. L. 1981, AJ, 86, 1619
———. 1984, Icarus, 60, 590
Wilbanks, T. M., Ade, P. A. R., Fischer, M. L., Holzapfel, W. L., & Lange, A. E. 1994, ApJ, 427, L75
Wright, E. L. 1979, ApJ, 232, 348
Zeldovich, Ya. B., & Sunyaev, R. A. 1968, Ap&SS, 4, 301